



Cite this: DOI: 10.1039/c5ta10690g

3-D binder-free graphene foam as a cathode for high capacity Li–O₂ batteries†

Chenjuan Liu,^a Reza Younesi,^a Cheuk-Wai Tai,^b Mario Valvo,^a Kristina Edström,^a Torbjörn Gustafsson^a and Jiefang Zhu^{*ac}

To provide energy densities higher than those of conventional Li-ion batteries, a Li–O₂ battery requires a cathode with high surface area to host large amounts of discharge product Li₂O₂. Therefore, reversible formation of discharge products needs to be investigated in Li–O₂ cells containing high surface area cathodes. In this study, a binder-free oxygen electrode consisting of a 3-D graphene structure on aluminum foam, with a high defect level ($I_D/I_G = 1.38$), was directly used as the oxygen electrode in Li–O₂ batteries, delivering a high capacity of about 9×10^4 mA h g⁻¹ (based on the weight of graphene) at the first full discharge using a current density of 100 mA g_{graphene}⁻¹. This performance is attributed to the 3-D porous structure of graphene foam providing both an abundance of available space for the deposition of discharge products and a high density of reactive sites for Li–O₂ reactions. Furthermore, the formation of discharge products with different morphologies and their decomposition upon charge were observed by SEM. Some nanoscaled LiOH particles embedded in the toroidal Li₂O₂ were detected by XRD and visualized by TEM. The amount of Li₂O₂ formed at the end of discharge was revealed by a titration method combined with UV-Vis spectroscopy analysis.

Received 28th December 2015

Accepted 10th April 2016

DOI: 10.1039/c5ta10690g

www.rsc.org/MaterialsA

Introduction

Li–O₂ batteries (often referred to as Li–air batteries) have attracted considerable interest due to their high theoretical specific energy (~ 3500 W h kg⁻¹), which is 5–10 times that of conventional Li-ion batteries (~ 380 W h kg⁻¹).^{1,2} However, the practical application of Li–O₂ batteries is not yet seen, due to many scientific and technological challenges. Firstly, in general the electrolyte solvents and salts are not stable during cycling.^{3,4} Secondly, the O₂ pathways are blocked by the precipitation of discharge products on the electrode eventually which limits the capacity of Li–O₂ batteries. Furthermore, high discharge–charge overpotentials⁵ and lack of efficient O₂ electrode design are still unsolved issues.⁶ Intensive research efforts have been made to overcome some of the aforementioned challenges by investigating different electrolytes,^{3,4} adding catalysts to reduce the overpotential,^{7,8} and designing a porous structure to provide high space utilization.^{9,10} There is still a critical need to understand the chemical processes in the Li–O₂ cell and promote its function despite all the progress achieved so far. Therefore, it is

necessary to design a Li–O₂ cell with a high surface area cathode coupled to a stable electrolyte to make a functioning Li–O₂ cell. Indeed, lately some electrolytes have been shown to be relatively stable in Li–O₂ cells with low surface area cathodes,^{11,12} but their stability in cells with high surface area cathodes is questionable.

It has been reported that graphene can enhance the cathode performance of Li–O₂ batteries due to its high electrical conductivity, unique morphology and highly porous structure with high surface area and pore volume after modification, which provide both diffusion channels for O₂ and active sites for the cathode reaction.^{10,13–15} Graphene can lower the overpotential and reduce the amount of side products such as LiRCO₃,^{15,16} compared to other kinds of carbon materials such as Vulcan XC-72, Ketjen Black, Super P and carbon nanotubes (CNTs). In addition, the unique 2-D structure and physical properties of graphene and its derivatives make them interesting as building blocks for constructing various 3-D porous architectures on a nanoscale.^{17–19} Recent work has shown that graphene oxide (GO) can be directly reduced by a number of metals, such as Fe,²⁰ Al²¹ and Cu,²² which opens a new possibility to assemble graphene on current collectors made of these metals. Among them, Al has been widely used as a current collector in Li–O₂ batteries.^{23–25} To maximize graphene utilization and oxygen diffusion, it can be highly efficient to use foam-structured Al current collectors, on which graphene foam can directly grow. By this method binder-free oxygen cathodes can be therefore designed and assembled as it is well-known that typical electrode binders such as, for example, polyvinylidene fluoride (PVDF) degrade in Li–O₂ cells.^{26–30}

^aDepartment of Chemistry – Ångström Laboratory, Uppsala University, Box 538, SE-751 21 Uppsala, Sweden. E-mail: jiefang.zhu@kemi.uu.se; Fax: +46 18 51 3548; Tel: +46 18 471 3722

^bDepartment of Materials and Environmental Chemistry, Stockholm University, SE 106 91 Stockholm, Sweden

^cState Key Laboratory of Fine Chemicals, Dalian University of Technology, Dalian 116024, China

† Electronic supplementary information (ESI) available. See DOI: 10.1039/c5ta10690g



In this work, we demonstrate a facile and efficient solution process followed by a low-temperature exfoliation to prepare a free-standing oxygen cathode. This cathode displays a 3-D structure arrangement of graphene foam derived from GO gel on an aluminum substrate (abbreviated as GF@Al). Without any additional binder and catalyst, GF@Al can be directly used as the O₂ electrode in Li–O₂ batteries. Meanwhile, the as-synthesized cathode exhibited a high specific capacity of up to 9×10^4 mA h g⁻¹ calculated based on the weight of graphene (or 60 mA h g⁻¹ based on the weight of the whole electrode) at a discharge current density of 100 mA g_{graphene}⁻¹. Stable charge–discharge cycling at a current density of 100 mA g_{graphene}⁻¹ showed an average over-potential of 1.17 V, and a specific electrode capacity of 1000 mA h g⁻¹ for 27 cycles. As the presented method also may be utilized to fabricate lightweight and high-performance freestanding electrodes with redox mediators or catalysts, the present approach clearly provides new possibilities for the manufacturing of binder free Li–O₂ batteries.

Results and discussion

Properties of GF@Al foam

The SEM micrographs of the electrodes presented in Fig. 1 show that graphene foam was formed both inside the pores of the Al foam and on the surface of the Al skeleton. Here, the Al foam serves both as the current collector and structure support for the graphene foam. The 3-D network structure, with open cages and honeycomb channels, facilitates O₂ gas diffusion and provides a large surface area for the deposition of the discharge product. Fig. 2a shows the Raman spectra of pristine GO and its derivative graphene foam (GF) reduced after heat treatment at 300 °C. The G band in GO is located at 1606 cm⁻¹, while for GF, the G band moves to 1595 cm⁻¹ (Table 1), which is close to the value of commercial graphite. This confirms that the reduction of GO occurred during the low temperature heating treatment. The D band, at 1351 and 1359 cm⁻¹, corresponding to GO and GF, respectively, indicates the defects of the sample and the size of the in-plane sp² domains. The intensity ratio of the D and G band (I_D/I_G) decreased from 1.54 in GO to 1.38 in GF (Table 1) due to the removal of oxygen-containing functional groups and the conversion to a more ordered graphitic structure. In the FTIR spectra (Fig. 2b), the peaks of GO around 1750 cm⁻¹, 1620 cm⁻¹, 1370 cm⁻¹, 1250 cm⁻¹ and 1070 cm⁻¹ correspond to

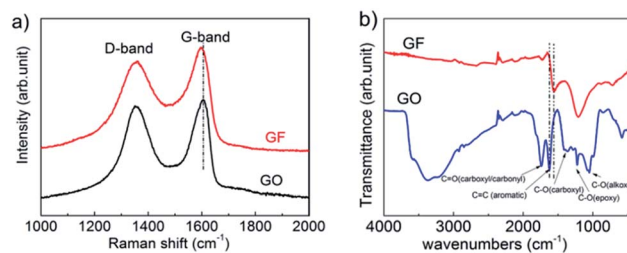


Fig. 2 (a) Raman and (b) FTIR spectra of GO and the as prepared GF.

carboxyl C=O, aromatic C=C, carboxyl C–O, epoxy C–O, and alkoxy C–O vibrations, respectively. After the heat treatment of GO at 300 °C, the alkoxy C–O peak disappeared in the spectrum of GF. Due to the reduction of oxygen-containing functional groups, the peak corresponding to aromatic C=C shifted to 1550 cm⁻¹ at lower frequency. This is also an indication of the reduction of GO. The epoxy C–O absorption increased from GO to GF, a sign of an increasing number of epoxy C–O groups in the GF sample. These functional groups are suggested to be beneficial for the reaction of absorbed O atoms with Li ions during the discharge process of a Li–O₂ battery.³¹

Performance of the GF@Al cathodes in Li–O₂ cells

The electrochemical characteristics of GF@Al electrodes for the discharge and charge processes in Li–O₂ cells were measured using cyclic voltammetry (CV) and galvanostatic cycling, as shown in Fig. 3. The ORR onset potentials for a conventional oxygen SP electrode and GF@Al are around 2.8 V and 3.0 V (*versus* Li⁺/Li in the cathodic scan), respectively. Compared with the SP electrode, the GF@Al electrode exhibits a higher ORR onset potential shift, indicating a lower ORR overpotential. Note that the following cathodic scan of GF@Al shows a broad peak until 2.0 V, indicating a continuous ORR. Besides, the GF@Al electrode shows more apparent ORR and OER peaks and higher peak current density during the cathodic and anodic scans. These findings show a higher catalytic activity of GF@Al compared to the SP electrode, assuming that the peaks originated from the ORR and OER. Galvanostatic measurements were carried out with a low cut-off voltage of 2.2 V using a current density of 100 mA g⁻¹ (normalized to the weight of graphene). The discharge capacity of the Al substrate was measured to be negligible (Fig. S1, ESI[†]), which means that the Al foam does not contribute to the capacity of the system. As shown in Fig. 3b, the GF@Al electrode exhibits a specific capacity of about 9×10^4 mA h g⁻¹ at a current density of 100 mA g⁻¹, corresponding to a specific energy of about 240 kW h kg_{graphene}⁻¹ (based on the average discharge voltage of 2.65 V).

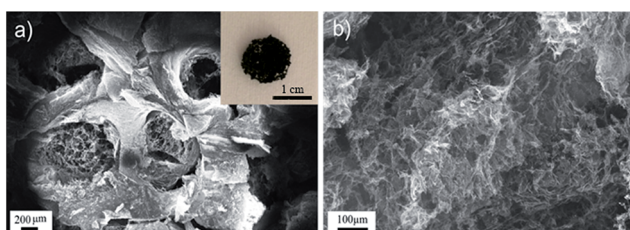


Fig. 1 (a) SEM image of graphene foam embedded in Al-foam, the inset shows a photograph of the whole electrode. (b) Enlarged SEM image of the GF@Al electrode.

Table 1 Summary of Raman spectroscopy results

Sample	I_D/I_G	G band position (cm ⁻¹)	$W_{F,D}$ (cm ⁻¹)
GO	1.54	1606	124.8
GF	1.38	1595	184.6



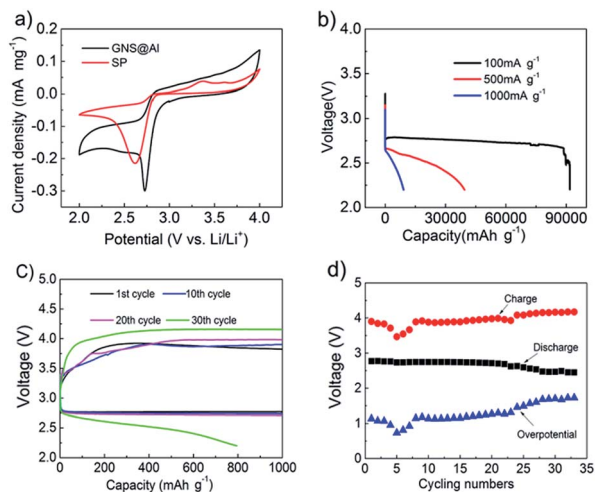


Fig. 3 Electrochemical characteristics of GF@Al in Li–O₂ cells using 1 M LiClO₄ in DMSO as the electrolyte. (a) CVs of GF@Al and Super P cathodes under an O₂ atmosphere for the second cycle at a constant scan rate of 0.1 mV s⁻¹. (b) Discharge curves of Li–O₂ cells with GF@Al at different current densities. (c) Charge–discharge curves and (d) cell voltages of Li–O₂ cells with GF@Al at a current density of 100 mA g⁻¹ with a capacity limitation of 1000 mA h g⁻¹.

To estimate the possible error originating from the weighing of deposited graphene on the Al foam, the highest mass of graphene obtained from 100% yield in the synthesis can also be considered (1.5 mg, see the Experimental section). Then, the discharge capacity is still as high as 2.4×10^4 mA h g⁻¹. Assuming that the graphene foam has a theoretical specific surface area of 2630 m² g⁻¹ and the coulombic efficiency of discharge is 100%, the thickness of the product will be about 13 nm at the end of discharge (calculation formula is presented in the ESI†). This calculated thickness is close to the reported “sudden death” value of ~5 to 10 nm, in which the tunneling current through the Li₂O₂ film can no longer support the electrochemical current.³² The discharge capacity and specific energy obtained from a 3-D graphene oxygen electrode containing a binder are 15 000 mA h g⁻¹ and 40 kW h kg_{carbon}⁻¹.³³ The high discharge capacity of our GF@Al electrode with a voltage limitation of 2.2 V is comparable to that of rGO prepared *via* a high temperature reduction process and discharged with a lower cut-off voltage of 2.0 V.³⁴ Even with a higher current density of up to 1000 mA g⁻¹, the GF@Al electrode can yield a discharge capacity of about 1×10^4 mA h g⁻¹. Fig. 3c and d show the discharge–charge curves and the working potential of a GF@Al electrode limited to a capacity of 1000 mA h g⁻¹ at a current density of 100 mA g⁻¹. The cell exhibited overpotentials between discharge–charge segments in the range of 1.06–1.27 V (Fig. 3c and d). As demonstrated in Fig. S2 (ESI)†, the GF@Al-based battery exhibited a lower discharge–charge voltage gap between 0.48 and 0.65 V under a capacity limitation of 500 mA h g⁻¹.

Identification of discharge products in the GF@Al electrode

The reaction products in the GF@Al electrodes after discharge and charge were examined by SEM, TEM, XRD and UV-Vis

spectroscopy. The SEM micrograph of the pristine GF@Al electrode shown in Fig. 4a demonstrates an open framework 3-D structure. After a full discharge to the cut-off voltage of 2.2 V, the open framework of the electrode was still maintained and the discharge products were uniformly deposited on both sides of the graphene electrode without clogging the pores, as shown in Fig. 4b. Most of the discharge products displayed a toroidal shape with a diameter of around 1 μm, which should be Li₂O₂ according to previous work.^{35–37} Fig. 4c shows the GF@Al electrode after the first discharge with a 1000 mA h g⁻¹ capacity limit. It reveals that the discharge products are uniformly deposited on the graphene surface, showing more toroidal-like products with rough surfaces and smaller diameters of around 100–500 nm. Fig. 4d shows the surface of the electrode after the first charge. By comparing with the results of Fig. 4c, we found that most of the toroidal products have disappeared and the bare graphene surface reappeared. From the SEM micrograph taken at higher magnification (the inset of Fig. 4d), it can be seen that the surface roughness of graphene is higher than that of the pristine electrode, which is most likely due to the incomplete decomposition of the discharge products or the

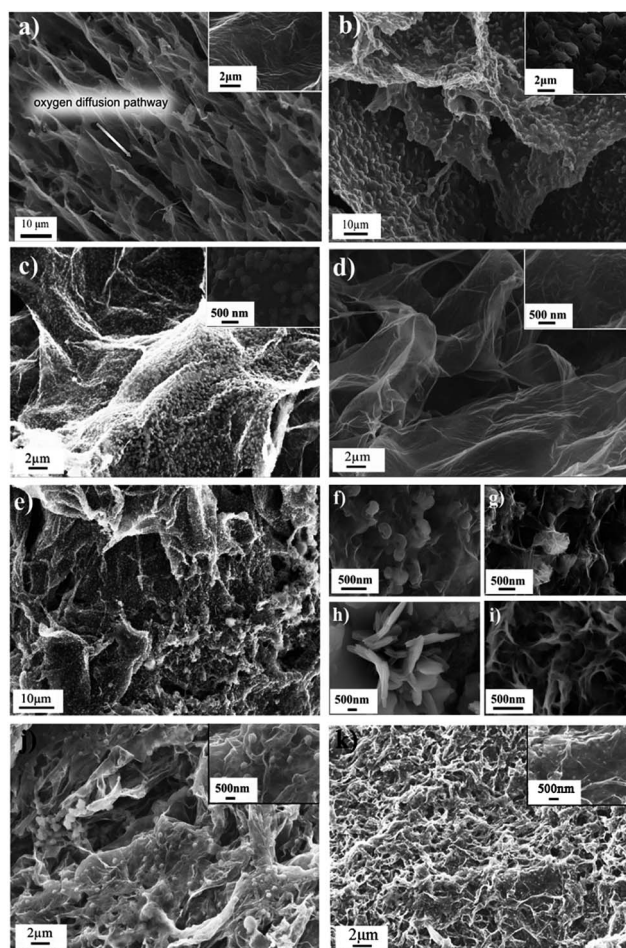


Fig. 4 SEM images of the GF@Al electrode (a) before and (b) after a full discharge, after (c) the 1st discharge, (d) 1st charge, and (e–i) 6th discharge, (j) half way of the 6th charge, and (k) after the 6th charge at 100 mA g⁻¹ current density.



deposition of a small amount of side products. After the 6th discharge, the GF@Al electrode surface is fully covered by discharge products, as shown in Fig. 4e. In contrast to previous studies,^{37–41} four morphologies of the products that have been reported to be Li₂O₂ produced under different discharge conditions were observed simultaneously at the same discharged electrode (see Fig. 4f–h). Fig. 4f shows the common toroidal-like morphology, which is also the primary morphology of the discharged products. Some spherical (Fig. 4g), disc shape (Fig. 4h), and nanosheet-like (Fig. 4i) morphologies of the discharge products were also observed after the 6th discharge, corresponding to the results of previous studies when using NiCo₂O₄ nanowires (1 M LiTFSI in DME as electrolyte),⁴² TiC (0.5 M LiClO₄ in DMSO as electrolyte)¹² and Ketjenblack carbon (1 M LiTFSI in TEGDME as electrolyte) as the cathode materials,⁴³ respectively. In this case, as the electrochemical environments should be the same for the same electrode, the formation of different morphologies may be related to defects or functional groups at the local surface structure of the graphene.

The SEM micrograph of the cycled electrode half way into the 6th charge, shown in Fig. 4j, indicates that most of the toroidal, disc, and nanosheet-like products disappear, but some spherical and film-like products still remain on the graphene surface. It can be deduced that during charging the toroidal, disc and nanosheet-like products decompose before the disappearance of spherical and film-like products. After the 6th full charge (Fig. 4k), minor amounts of reaction products still remain on the graphene, but the size of the spherical products is less than 100 nm. Comparing Fig. 4e, j and k with Fig. 4c and d, one can conclude that after several cycles the electrode becomes more compact and both surface roughness and thickness of graphene increase. This is due to the accumulation of discharge and side products, which limits the reversibility of the Li–O₂ battery.

The products formed after the full discharge were further investigated by TEM. Fig. 5a shows a bright-field TEM (BF-TEM) micrograph of toroidal products after full discharge. In the selected area electron diffraction (SAED) pattern shown in Fig. 5b recorded at the same sample spot, the ring pattern reveals that the toroidal Li₂O₂ is poly-crystalline. The observed diffraction rings are indexed to 002, 100 and 101 of Li₂O₂ (ICSD file no. 01-074-0115 9-355). The nanosized grains and their boundaries in a toroidal Li₂O₂ particle are revealed by the variation of contrasts in Fig. 5c. Some reflections belonging to LiOH are also observed in the SAED pattern (Fig. 5d) taken from the big toroidal Li₂O₂, of which the BF-TEM image is shown in Fig. 5e. In the dark-field TEM image (*g* = 211 of LiOH) shown in Fig. 5f, the bright contrasts reveal some LiOH particles incorporated in the toroidal Li₂O₂. The product LiOH has been reported earlier when using DMSO as the electrolyte.^{36,44–47} However, LiOH and Li₂O₂ cannot be simply distinguished by their morphology. The TEM results clearly confirm the coexistence of LiOH and Li₂O₂.

XRD was also used to further identify the discharge products. As shown in Fig. 6, the diffraction peaks (32.7°, 35.0°, and 58.7° in 2θ) clearly confirm the formation of Li₂O₂ after full discharge. The product of LiOH was also detected, which is consistent with

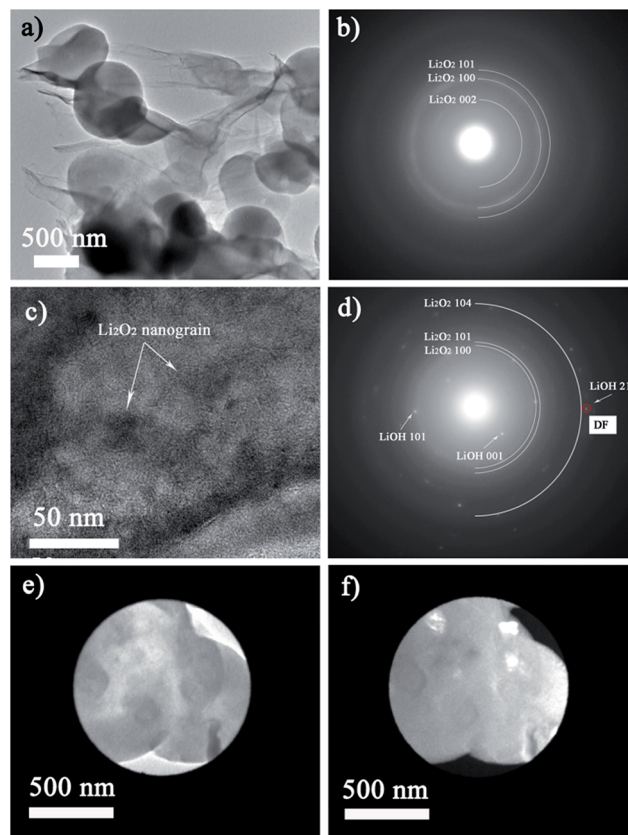


Fig. 5 (a) BF-TEM image of the O₂ electrode after the full discharge. (b) SAED pattern corresponding to the region shown in (a). (c) BF-TEM image of toroidal Li₂O₂ taken at higher magnification. (d) SAED pattern of the selected area shown in (c). (e) BF-TEM image of the toroidal Li₂O₂ and (f) DF-TEM of LiOH (*g* = 211).

the TEM results, while neither Li₂O₂ nor LiOH peaks appeared at the end of first charge, which is in agreement with the SEM results. A likely cause of the formation of LiOH is a side reaction of the DMSO-based electrolyte as several previous studies reported that Li₂O₂ reacts with DMSO to form LiOH.^{46,48} The degradation of DMSO by Li₂O₂ could be explained by the chemistry of DMSO and Li₂O₂. The methyl group in DMSO is

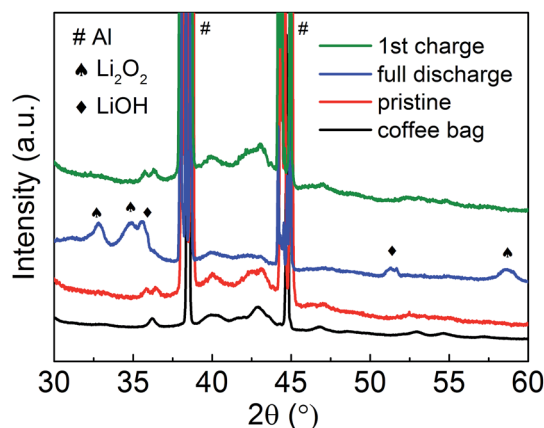


Fig. 6 XRD patterns of pristine, discharged and charged cathodes.



weakly acidic, while Li_2O_2 is a strong base that can abstract protons from it to form hydroperoxy radicals. Therefore, DMSO could degrade to a dimethyl anion and a hydroperoxy radical because of abstraction of a proton by Li_2O_2 to form LiOH .⁴⁶ Another explanation could be the high polarity of the DMSO solvent that makes it more miscible with water than many other organic solvents, which leads to the formation of LiOH .⁴⁴ In order to further investigate the amount of Li_2O_2 formed after a full discharge, a UV-Vis spectroscopy analysis was employed by using a reaction between Li_2O_2 and H_2O to produce H_2O_2 .⁴⁹ According to the absorption curve (see ESI† for the details of the principle), the yield of Li_2O_2 ($Y_{\text{Li}_2\text{O}_2}$, the amount of Li_2O_2 produced divided by the amount of Li_2O_2 expected given by the coulometry; see Table S1†) was estimated to be less than 40%. However, it should be noted that the results may be underestimated, due to the catalytic effect of the pristine electrode, the loss of the electrode material and the tendency of H_2O_2 to degrade to H_2O and O_2 during titration. With a conventional oxygen electrode containing a mixture of Super P carbon black and a binder that delivers almost 10 times lower capacity, $Y_{\text{Li}_2\text{O}_2}$ is around 50%. This suggests that the lower $Y_{\text{Li}_2\text{O}_2}$ in the high capacity GF@Al electrode is likely due to a reaction between Li_2O_2 and DMSO, as DMSO degrades in contact with Li_2O_2 .^{47,48} In order to further investigate the parasitic reactions, XPS analyses were carried out. The C 1s XPS spectra (Fig. S3†) showed that some decomposition products containing ether and carboxylate bonds formed on the surface of the graphene electrode after the 1st discharge. The results also revealed a noticeable contribution from the carbonate ($-\text{CO}_3$) decomposition product to the C 1s spectrum of the graphene electrode after the 7th discharge. Similarly, the Cl 2p spectra showed that LiClO_4 salt decomposition has minor contribution after the 1st discharge but increases after the 7th discharge. The formation of carbonate species such as Li_2CO_3 might be due to (i) the decomposition of the electrolyte or (ii) the side reactions between Li_2O_2 and the graphene electrode, and we cannot exclude either of them at this stage.

The above results demonstrate that the GF@Al electrode can provide a high capacity with the existence of both Li_2O_2 and LiOH . However, the efficiency and the life span of the GF@Al electrode can be improved in cells with a stable electrolyte and good redox mediator, such as LiI , which could cycle both Li_2O_2 and LiOH for practical applications.^{50,51}

Conclusions

Binder-free, 3-D network GF@Al electrodes were successfully prepared by the assembly of GO and using a substrate-assisted reduction method. Without any binder, GF@Al was directly used as the oxygen electrode for $\text{Li}-\text{O}_2$ batteries, which delivered a full discharge capacity of about $9 \times 10^4 \text{ mA h g}^{-1}$ (based on the weight of graphene) at a current density of 100 mA g^{-1} in $\text{Li}-\text{O}_2$ cells. The low density packed 3-D network structure facilitates O_2 diffusion in the electrode and provides enough voids for the deposition of discharge. The existence of different morphologies of discharge products indicates the complexity during battery cycling. Nanoscaled LiOH incorporated into the

toroidal Li_2O_2 in the fully discharged electrode was clearly visualized by TEM analysis. XRD and UV-Vis spectroscopy results further confirm the incomplete formation of Li_2O_2 with the co-existence of LiOH during discharge. This work shows a new design of a binder-free electrode with high surface area to achieve a high capacity, which is one of the main requirements for $\text{Li}-\text{O}_2$ cells, but it also indicates the formation of LiOH when large surface area graphene is in contact with the electrolyte solution.

Experimental

Preparation of the GF@Al electrodes

The fabrication process of the GF@Al electrode is schematically illustrated in Fig. 7. A 3-D structured GO network was formed on Al foam (thickness of 3.2 mm and diameter of 12 mm with 93% porosity, purchased from GoodFellow) using a substrate-assisted reduction and assembly of GO (SARA-GO) method.⁵² The Al foam was initially sonicated in acetone, and rinsed with DI water, to remove any organic compounds from the surface. The clean Al foam was then exposed to 3 mL of 1 g L^{-1} GO aqueous (supplied from Sigma-Aldrich) for 12 h under ambient conditions (step i in Fig. 7). GO was assembled on the Al foam in a gel network (step ii in Fig. 7), and then the water was removed from the pores of the gel network by freeze-drying technology to get a 3-D GO/reduced graphene oxide (rGO) network. The product was (step iii in Fig. 7) further annealed *via* a low-temperature exfoliation approach (at $300 \text{ }^\circ\text{C}$ for 24 h) under vacuum ($<10^{-2}$ mbar)⁵³ to thermally reduce the GO. Finally, the GF@Al electrodes were directly used as O_2 electrodes in $\text{Li}-\text{O}_2$ batteries. The mass of graphene in each electrode was about 0.4 mg. Note that the maximum mass of graphene would be 1.5 mg if all the GO in solution had been reduced and stayed on the surface of the Al foam. The values of the actual measured mass and the highest

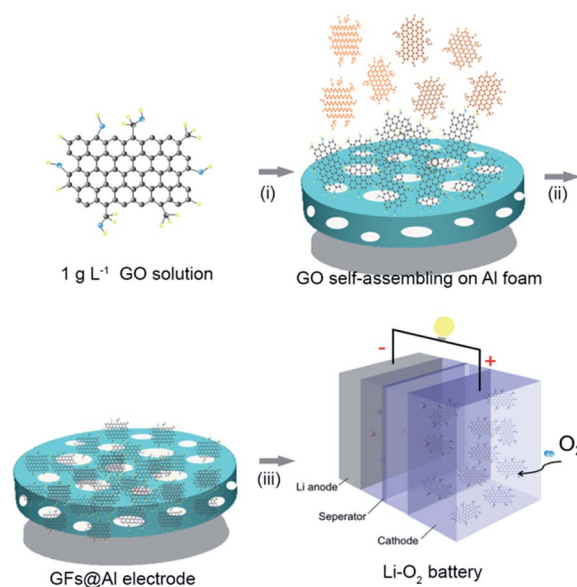


Fig. 7 (a) Schematic illustration of the assembly process and the architecture of the obtained freestanding of the GF@Al electrode.



theoretical mass of graphene are used in the Results and discussion section for the estimation of specific capacity. For comparison and as a reference, traditional Super P electrodes were prepared by mixing Super P carbon (Erachem Comilog) and PVDF (Arkema) with a weight ratio of 9 : 1 in an NMP solvent and casting on an Al mesh.

Material characterization

SEM and TEM measurements were carried out using a Zeiss 1550 with an in-lens secondary detector and a JEOL JEM-2100F microscope, respectively. The TEM samples were prepared in a glovebox and loaded into a JEOL vacuum transfer holder. The TEM images and selected-area electron diffraction (SAED) patterns were recorded by using a Gatan Ultrascan 1000 and an Orius 200D camera, respectively. XRD patterns were obtained on a STOE transmission diffractometer operating with Cu K α 1 radiation. The discharged electrodes for XRD analysis were prepared in an Ar-filled glovebox and sealed in pouch cells to avoid exposure to ambient air during the measurements. FTIR measurements were carried out on a Perkin Elmer attenuated total reflectance-Fourier transform infrared (ATR-FTIR) spectrometer. Raman spectra were measured and collected using a Renishaw Ramascope equipped with a Leica LM optical microscope, a CCD camera and an Ar ion laser ($\lambda = 514.5$ nm) source.

Electrochemical characterization

Dimethyl sulfoxide (DMSO) (>99.5%) and battery grade lithium perchlorate (LiClO₄) (Aldrich 99.99%) were purchased from Sigma-Aldrich. DMSO was dried over 4 Å molecular sieves for several days before use and LiClO₄ was dried under vacuum (at 120 °C for 24 h). 1 M LiClO₄/DMSO electrolyte was prepared in an Ar-filled glovebox with O₂ and H₂O contents less than 5 ppm. The cells were assembled (based on a Swagelok type design) inside an Ar-filled glovebox (details of the cell assembly have been presented in ref. 27). Li–O₂ cells were composed of a Li metal foil anode (12 mm in diameter, 0.25 mm thick), a piece of glass fiber separator (14 mm diameter), an electrolyte (1 M LiClO₄ in DMSO), and the as-prepared GF@Al cathode. With an exception of the cathode side which was exposed to a pure O₂ atmosphere, the cells were gas-tightened, and kept for 5 hours before testing. Discharge/charge measurements were performed on a Digatron BTS-600 system at room temperature.

The Li–O₂ cells were disassembled in an Ar-filled glovebox after cycling for SEM, TEM, XRD, and UV-Vis spectroscopic analyses. The remaining electrolyte was removed from the cathode surface with a clean tissue. The cathodes were further washed with dimethyl carbonate (DMC), and dried at 120 °C in a vacuum oven overnight.

Acknowledgements

The authors gratefully appreciate the financial support by Swedish Research Council (2012-4681 and 2011-6512), Swedish Energy Agency, Ångpanneföreningen's Foundation for Research and Development, J. Gust. Richert Foundation, the State Key

Laboratory of Fine Chemicals (KF1413) and China Scholarship Council. The Knut and Alice Wallenberg (KAW) Foundation is acknowledged for providing the electron microscopy facilities at Stockholm University.

Notes and references

- 1 P. G. Bruce, S. A. Freunberger, L. J. Hardwick and J. M. Tarascon, *Nat. Mater.*, 2012, **11**, 19–29.
- 2 J. M. Tarascon and M. Armand, *Nature*, 2001, **414**, 359–367.
- 3 R. Younesi, M. Hahlin, F. Björefors, P. Johansson and K. Edström, *Chem. Mater.*, 2013, **25**, 77–84.
- 4 R. Younesi, G. M. Veith, P. Johansson, K. Edström and T. Vegge, *Energy Environ. Sci.*, 2015, **8**, 1905–1922.
- 5 F. Li, T. Zhang and H. Zhou, *Energy Environ. Sci.*, 2013, **6**, 1125.
- 6 S. Liu, Z. Wang, C. Yu, Z. Zhao, X. Fan, Z. Ling and J. Qiu, *J. Mater. Chem. A*, 2013, **1**, 12033.
- 7 J. Liu, R. Younesi, T. Gustafsson, K. Edström and J. Zhu, *Nano Energy*, 2014, **10**, 19–27.
- 8 D. Sun, Y. Shen, W. Zhang, L. Yu, Z. Yi, W. Yin, D. Wang, Y. Huang, J. Wang, D. Wang and J. B. Goodenough, *J. Am. Chem. Soc.*, 2014, **136**, 8941–8946.
- 9 H. D. Lim, K. Y. Park, H. Song, E. Y. Jang, H. Gwon, J. Kim, Y. H. Kim, M. D. Lima, R. Ovalle Robles, X. Lepro, R. H. Baughman and K. Kang, *Adv. Mater.*, 2013, **25**, 1348–1352.
- 10 J. Xiao, D. H. Mei, X. L. Li, W. Xu, D. Y. Wang, G. L. Graff, W. D. Bennett, Z. M. Nie, L. V. Saraf, I. A. Aksay, J. Liu and J. G. Zhang, *Nano Lett.*, 2011, **11**, 5071–5078.
- 11 B. D. McCloskey, A. Valery, A. C. Luntz, S. R. Gowda, G. M. Wallraff, J. M. Garcia, T. Mori and L. E. Krupp, *J. Phys. Chem. Lett.*, 2013, **4**, 2989–2993.
- 12 M. M. Ottakam Thotiyl, S. A. Freunberger, Z. Peng, Y. Chen, Z. Liu and P. G. Bruce, *Nat. Mater.*, 2013, **12**, 1050–1056.
- 13 Y. Li, J. Wang, X. Li, D. Geng, R. Li and X. Sun, *Chem. Commun.*, 2011, **47**, 9438–9440.
- 14 H. R. Byon, B. M. Gallant, S. W. Lee and Y. Shao-Horn, *Adv. Funct. Mater.*, 2013, **23**, 1037–1045.
- 15 B. Sun, B. Wang, D. Su, L. Xiao, H. Ahn and G. Wang, *Carbon*, 2012, **50**, 727–733.
- 16 S. Y. Kim, H. T. Lee and K. B. Kim, *Phys. Chem. Chem. Phys.*, 2013, **15**, 20262–20271.
- 17 Z. P. Chen, W. C. Ren, L. B. Gao, B. L. Liu, S. F. Pei and H. Cheng, *Nat. Mater.*, 2011, **10**, 424–428.
- 18 Z. Niu, J. Chen, H. H. Hng, J. Ma and X. Chen, *Adv. Mater.*, 2012, **24**, 4144–4150.
- 19 J. Biener, S. Dasgupta, L. Shao, D. Wang, M. A. Worsley, A. Wittstock, J. R. Lee, M. M. Biener, C. A. Orme, S. O. Kucheyev, B. C. Wood, T. M. Willey, A. V. Hamza, J. Weissmuller, H. Hahn and T. F. Baumann, *Adv. Mater.*, 2012, **24**, 5083–5087.
- 20 Z. J. Fan, W. Kai, J. Yan, T. Wei, L. J. Zhi, J. Feng, Y. M. Ren, L. P. Song and F. Wei, *ACS Nano*, 2011, **5**, 191–198.
- 21 Z. J. Fan, K. Wang, T. Wei, J. Yan, L. P. Song and B. Shao, *Carbon*, 2010, **48**, 1686–1689.



- 22 X. B. Cao, D. P. Qi, S. Y. Yin, J. Bu, F. J. Li, C. F. Goh, S. Zhang and X. D. Chen, *Adv. Mater.*, 2013, **25**, 2957–2962.
- 23 T. Ogasawara, A. Debart, M. Holzapfel, P. Novak and P. G. Bruce, *J. Am. Chem. Soc.*, 2006, **128**, 1390–1393.
- 24 Y.-C. Lu, H. Gasteiger, M. Parent, V. Chiloyan and Y. Shao-Horn, *Electrochem. Solid-State Lett.*, 2010, **13**, A69–A72.
- 25 J. Liu, M. Roberts, R. Younesi, M. Dahbi, K. Edström, T. Gustafsson and J. Zhu, *J. Phys. Chem. Lett.*, 2013, **4**, 4045–4050.
- 26 R. Black, S. H. Oh, J. H. Lee, T. Yim, B. Adams and L. F. Nazar, *J. Am. Chem. Soc.*, 2012, **134**, 2902–2905.
- 27 R. Younesi, M. Hahlin and K. Edstrom, *ACS Appl. Mater. Interfaces*, 2013, **5**, 1333–1341.
- 28 R. Younesi, M. Hahlin, M. Treskow, J. Scheers, P. Johansson and K. Edström, *J. Phys. Chem. C*, 2012, **116**, 18597–18604.
- 29 W. Xu, K. Xu, V. V. Viswanathan, S. A. Towne, J. S. Hardy, J. Xiao, Z. Nie, D. Hu, D. Wang and J.-G. Zhang, *J. Power Sources*, 2011, **196**, 9631–9639.
- 30 C. V. Amanchukwu, J. R. Harding, Y. Shao-Horn and P. T. Hammond, *Chem. Mater.*, 2015, **27**, 550–561.
- 31 H. J. Yan, B. Xu, S. Q. Shi and C. Y. Ouyang, *J. Appl. Phys.*, 2012, **112**, 104316.
- 32 V. Viswanathan, K. S. Thygesen, J. S. Hummelshøj, J. K. Nørskov, G. Girishkumar, B. D. McCloskey and A. C. Luntz, *J. Chem. Phys.*, 2011, **135**, 214704.
- 33 J. Xiao, D. Mei, X. Li, W. Xu, D. Wang, G. L. Graff, W. D. Bennett, Z. Nie, L. V. Saraf, I. A. Aksay, J. Liu and J. G. Zhang, *Nano Lett.*, 2011, **11**, 5071–5078.
- 34 M. M. Storm, M. Overgaard, R. Younesi, N. E. A. Reeler, T. Vosch, U. G. Nielsen, K. Edström and P. Norby, *Carbon*, 2015, **85**, 233–244.
- 35 R. R. Mitchell, B. M. Gallant, C. V. Thompson and Y. Shao-Horn, *Energy Environ. Sci.*, 2011, **4**, 2952.
- 36 D. Xu, Z. L. Wang, J. J. Xu, L. L. Zhang and X. B. Zhang, *Chem. Commun.*, 2012, **48**, 6948–6950.
- 37 J. Lu, L. Cheng, K. C. Lau, E. Tyo, X. Luo, J. Wen, D. Miller, R. S. Assary, H. H. Wang, P. Redfern, H. Wu, J. B. Park, Y. K. Sun, S. Vajda, K. Amine and L. A. Curtiss, *Nat. Commun.*, 2014, **5**, 4895.
- 38 B. D. Adams, C. Radtke, R. Black, M. L. Trudeau, K. Zaghbi and L. F. Nazar, *Energy Environ. Sci.*, 2013, **6**, 1772.
- 39 N. B. Aetukuri, B. D. McCloskey, J. M. Garcia, L. E. Krupp, V. Viswanathan and A. C. Luntz, *Nat. Chem.*, 2015, **7**, 50–56.
- 40 Y.-C. Lu, D. G. Kwabi, K. P. C. Yao, J. R. Harding, J. Zhou, L. Zuin and Y. Shao-Horn, *Energy Environ. Sci.*, 2011, **4**, 2999.
- 41 Y. Li, J. Wang, X. Li, D. Geng, M. N. Banis, Y. Tang, D. Wang, R. Li, T.-K. Sham and X. Sun, *J. Mater. Chem.*, 2012, **22**, 20170.
- 42 W. M. Liu, T. T. Gao, Y. Yang, Q. Sun and Z. W. Fu, *Phys. Chem. Chem. Phys.*, 2013, **15**, 15806–15810.
- 43 Z. Guo, X. Dong, S. Yuan, Y. Wang and Y. Xia, *J. Power Sources*, 2014, **264**, 1–7.
- 44 D. Xu, Z. L. Wang, J. J. Xu, L. L. Zhang, L. M. Wang and X. B. Zhang, *Chem. Commun.*, 2012, **48**, 11674–11676.
- 45 B. Sun, P. Munroe and G. Wang, *Sci. Rep.*, 2013, **3**, 2247.
- 46 D. Sharon, M. Afri, M. Noked, A. Garsuch, A. A. Frimer and D. Aurbach, *J. Phys. Chem. Lett.*, 2013, **4**, 3115–3119.
- 47 M. J. Trahan, S. Mukerjee, E. J. Plichta, M. A. Hendrickson and K. M. Abraham, *J. Electrochem. Soc.*, 2012, **160**, A259–A267.
- 48 R. Younesi, P. Norby and T. Vegge, *ECS Electrochem. Lett.*, 2014, **3**, A15–A18.
- 49 P. Hartmann, C. L. Bender, J. Sann, A. K. Durr, M. Jansen, J. Janek and P. Adelhelm, *Phys. Chem. Chem. Phys.*, 2013, **15**, 11661–11672.
- 50 H. D. Lim, H. Song, J. Kim, H. Gwon, Y. Bae, K. Y. Park, J. Hong, H. Kim, T. Kim, Y. H. Kim, X. Lepro, R. Ovalle-Robles, R. H. Baughman and K. Kang, *Angew. Chem.*, 2014, **53**, 3926–3931.
- 51 T. Liu, M. Leskes, W. Yu, A. J. Moore, L. Zhou, P. M. Bayley, G. Kim and C. P. Grey, *Science*, 2015, **350**, 530–533.
- 52 C. Hu, X. Zhai, L. Liu, Y. Zhao, L. Jiang and L. Qu, *Sci. Rep.*, 2013, **3**, 2065.
- 53 W. Lv, D. M. Tang, Y. B. He, C. H. You, Z. Q. Shi, X. C. Chen, C. M. Chen, P. X. Hou, C. Liu and Q. H. Yang, *ACS Nano*, 2009, **3**, 3730–3736.

